Numerical simulations of marble sulfation

Armando Coco, Marco Donatelli, Matteo Semplice, and Stefano Serra Capizzano

Abstract In this chapter we describe some computational techniques to approximate the evolution of gypsum crusts on marble monuments. Mathematical models of this phenomenon are typically based on partial differential equations and here we deliberately consider a quite simple one, so that we can focus on the numerical techniques that can be used to overcome the main difficulties of this kind of computations, namely the efficiency of the timestepping procedure and the complexity of the computational domains in real-world cases. First, the design of optimal preconditioners for Cartesian grid discretizations is reviewed. Then, we illustrate a technique to deal with non Cartesian domains by described via a level-set function. The chapter ends with a study of the influence of the surface curvature on the growth of the gypsum crust, that generalizes earlier analytical one-dimensional results.

1 Introduction

An accurate quantitative forecasts of the evolution of a work of art in a polluted environment would allow to better schedule monitoring, preservation and restoration

Armando Coco
School of Engineering, Computing and Mathematics, Oxford Brookes University, Wheatley campus, Oxford (UK) e-mail: acoco@brookes.ac.uk

Marco Donatelli
Dipartimento di Scienza e Alta Tecnologia, Università dell'Insubria, Via Valleggio 11, 22100 Como (Italy) e-mail: marco.donatelli@uninsubria.it

Matteo Semplice
Dipartimento di Scienza e Alta Tecnologia, Università dell'Insubria, Via Valleggio 11, 22100 Como (Italy) e-mail: matteo.semplice@uninsubria.it

Stefano Serra Capizzano
Dipartimento di Scienze Umane e dell'Innovazione per il territorio, Università dell'Insubria, via Bossi 5, 22100 Como (Italy) e-mail: stefano.serracapizzano@uninsubria.it

activities in the management of the cultural heritage [11]. In [21] various mathematical models for the interaction of the material of a work of art with chemicals in the surrounding environment have been compared and the employment of models, based on partial differential equations (PDEs), has been advocated for the next generation of models with regulatory powers.

Typical differential models in this field turn out to be systems of reaction-diffusion equations that describe the penetration of chemicals in the work of art and their reaction with its pristine material. As an example, here we focus on the sulfation of marble, for which many models of different complexity and accuracy have been proposed [2, 1, 4, 6, 20]. Although the later ones can describe the phenomenon more accurately, here we will consider the simplest proposed in [2], since it already contains the main difficulties related to the computation of the solutions.

The long-time behaviour of the solutions of the PDE introduced in [2] has been studied in the same paper and an experimental validation of the one-dimensional model has been performed in [17]. Such results can of course give important insights on sulfation: for example it was shown that the thickness of the crust evolves as the square root of the elapsed time, thus being much faster in the early stages, when the crust is still thin. This adds quantitative support to the qualitative knowledge, well spread among practitioners, that the crust should not be removed entirely when restoring a piece of art.

Of course, the long-time asymptotics of the one-dimensional model are inadequate to give precise quantitative information in the short time-scale and in general on the state of a complex piece of art like a statue, which is inherently three-dimensional and has a complex geometry. In order to allow the application of differential models to real–world cases, the numerical approximation of the solution of the system of PDEs in complex geometries must be sought and a full workflow from the measurement of the piece of art to the computation of the model and to the representation of its solutions in a form that is useful for the management of cultural heritage must be devised.

In this work we focus on the numerical solution of the model of [2], recalled in §2, revising previous work of the authors on this subject. As a first step beyond the one-dimensional discretizations two-dimensional Cartesian domains were considered in [22] and a better work/precision efficiency was obtained in [13] with the use of non-uniform Cartesian discretizations. These are described in §3. Further, arbitrary domains have been considered through a level-set approach in [10], which is the subject of §4. In §5 the latter method is applied to the study of the dependence of the asymptotic speed of propagation of the crust front as a function of the surface curvature radius. Finally §6 summarizes our findings and indicates some directions for future research in this field.

2 Mathematical model

The mathematical model presented in [2] captures the essence of the sulfation process by considering a physical domain Ω and two real valued functions $s(t,\mathbf{x})$ and $c(t,\mathbf{x})$, representing respectively concentration of the pristine stone and of the gaseous pollutant at time $t \geq 0$ and at the point $\mathbf{x} \in \Omega$.

The evolution of s and c is prescribed in order to mimic the simplified reaction

$$CaCO_3 + SO_2 + \frac{1}{2}O_2 + 2H_2O \longrightarrow CaSO_4 \cdot 2H_2O + CO_2$$

and is given by

$$\begin{cases} \dfrac{\partial\,(\phi(c)s)}{\partial t} = -\dfrac{a}{m_c}\phi(c)\,s\,c + d\,\nabla\cdot(\phi(c)\nabla s) & \text{in } \Omega\times[0,T], \\ \dfrac{\partial c}{\partial t} = -\dfrac{a}{m_s}\phi(c)\,s\,c & \text{in } \Omega\times[0,T], \end{cases} \tag{1}$$

where c represents the concentration of $CaCO_3$, s the concentration of SO_2 and $1-c(t,\mathbf{x})$ the concentration of $CaSO_4 \cdot 2H_2O$ (gypsum), see [2] for the derivation of the model.

In the equations, ϕ represents the porosity of the material, which controls the diffusion of the gas in the pores. Since marble and gypsum have different porosities, ϕ is a function of $c(\mathbf{x},t)$, making the diffusion equation a nonlinear one. For simplicity, as in [2], we assume that $\phi(c(\mathbf{x},t)) = \alpha\,c(\mathbf{x},t) + \beta$, with $\alpha = 0.01$ and $\beta = 0.1$. Of course, more complex relations may be employed, since our methods do not rely strongly on a particular functional form for ϕ. The first terms on the right-hand-side of each PDE represent the consumption of $CaCO_3$ and SO_2 by the reaction, which proceeds at speed a; furthermre m_c and m_s take into account the masses of the reactants. The final term of the first equation of (1) represents instead the diffusion of SO_2 in the domain, which is modelled as a Fick diffusion process with coefficient $\phi(c)$ and further regulated by the constant d. We point out that a and d should be set in accordance to environmental conditions, at least temperature and humidity.

System (1) must be supplemented with suitable initial and boundary conditions, see also [2]. For example, when dealing with a pristine work of art, one may assume that $c(\mathbf{x},0) = 1$ and that $s(\mathbf{x},0) = 0$. When the region Ω coincides with the entire monument, a (possibly time dependent) Dirichlet boundary condition for s is appropriate to represent the level of pullution in the surrounding air. If the computational domain is restricted to a portion of the monument (see e.g. Fig. 1), homogeneous Neumann boundary conditions are applied on the part of $\partial\Omega$ that is inside the monument. Finally, no boundary conditions are needed for c, but, when artificial ones are required by numerical methods, homogeneous Neumann boundary conditions are chosen.

3 Numerical approximation for Cartesian domains

A typical case where a Cartesian domain is useful is the study of the square edge of a monument, illustrated in Fig. 1a. Assuming that the edge coincides with the z axis, we can compute this situation by considering a rectangular region $\Omega = (0, L) \times (0, L)$ in the (x, y) plane: two sides of Ω are in contact with the polluted air (cyan dots) and the two opposite sides are inside the marble (pink hatching).

Grid setup This case can be efficiently dealt with spatial discretizations based on a staggered grid arrangement of the variables; in particular, s variables are stored at the nodes of a Cartesian grid, while c variables are stored on the dual grid. The main grid can be uniform as in [22] or non uniform as in [13] and is illustrated in Fig. 1b.

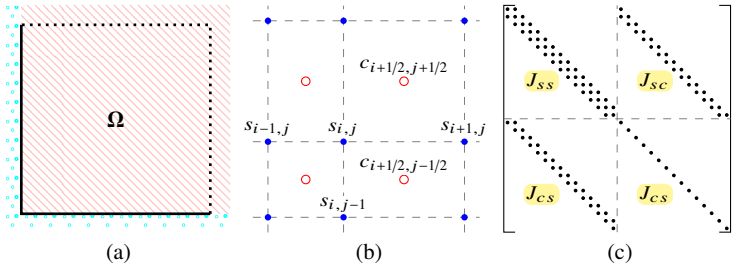

Fig. 1 (a) Computational domain. (b) Staggered grid arrangement. (c) Jacobian sparsity pattern for the 1D case.

Spatial discretization At any point inside the domain, we approximate the right-hand-side of (1) by standard finite difference formulas. In the case of a uniform grid,

$$\mathrm{L}_h^s(\mathbf{s},\mathbf{c})\Big|_{i,j} = -\frac{a}{m_c}\phi(\hat{c}_{ij})\, s_{ij}\, \hat{c}_{ij} + d \sum \phi(c_{i\pm 1/2, j\pm 1/2})\frac{s_{i\pm1,j\pm1} - s_{ij}}{h^2} \tag{2a}$$

$$\mathrm{L}_h^c(\mathbf{s},\mathbf{c})\Big|_{i+1/2,j+1/2} = -\frac{a}{m_s}\phi\left(c_{i+1/2,j+1/2}\right)\, \hat{s}_{i+1/2,j+1/2}\, c_{i+1/2,j+1/2}, \tag{2b}$$

where h is the grid spacing and the sum contains four terms, one for each of the first neighbours $s_{i+1,j}$, $s_{i-1,j}$, $s_{i,j+1}$ and $s_{i,j-1}$. The $\hat{s}$ and $\hat{c}$ quantities refer to averages of the s and c variables computed at, respectively, c and s nodes [22]. In case of non uniform grids, formulas (2) should of course be modified taking into account the actual distance between each node so that second order accuracy is preserved, as explained in [13].

Time discretization Time advancement of the solution can then be computed by the Crank-Nicolson scheme, i.e. s_{ij}^{n+1} and c_{ij}^{n+1} are computed by solving the coupled system of equations

$$0 = F^s_{ij} = \frac{\phi\left(\hat{c}^{(n+1)}_{ij}\right) s^{(n+1)}_{ij} - \phi\left(\hat{c}^{(n)}_{ij}\right) s^{(n)}_{ij}}{\Delta t} - \frac{\mathrm{L}^s_h(\mathbf{s}^{(n)}, \mathbf{c}^{(n)}) + \mathrm{L}^s_h(\mathbf{s}^{(n+1)}, \mathbf{c}^{(n+1)})}{2} \tag{3a}$$

$$0 = F^c_{ij} = \frac{c^{(n+1)}_{i+1/2,j+1/2} - c^{(n)}_{i+1/2,j+1/2}}{\Delta t} - \frac{\mathrm{L}^c_h(\mathbf{s}^{(n)}, \mathbf{c}^{(n)}) + \mathrm{L}^c_h(\mathbf{s}^{(n+1)}, \mathbf{c}^{(n+1)})}{2}\,. \tag{3b}$$

The number of variables in the previous system grows with the inverse of the grid spacing as $O(1/h^d)$ in d spatial dimensions, quickly leading to a very large number of unknowns in two and three space dimensions.

Boundary conditions In the case of rectangular or otherwise logically Cartesian domains, equations (3) are solved for all grid points and equations (2) are modified accordingly to the boundary conditions in the first layer of grid points close to the grid boundary, as detalied in [22, 13].

Nonlinear solver System (3) is a nonlinear system of equations that must be solved at each time step in order to advance the solution from time t^n to time t^{n+1}. Under a restriction of type $\Delta t = O(h)$, this can be achieved with the Newton-Raphson method [12, 22]. In particular we initialize the approximate solution with the previous time step values, i.e. $s^{n+1,0} = s^n$ and $c^{n+1,0} = c^n$, and then compute the iterations

$$\begin{pmatrix} s \\ c \end{pmatrix}^{n+1,k} = \begin{pmatrix} s \\ c \end{pmatrix}^{n+1,k} - \begin{pmatrix} \Delta s \\ \Delta c \end{pmatrix} \tag{4a}$$

where the increment is the solution of the linear system

$$J \begin{pmatrix} \Delta s \\ \Delta c \end{pmatrix} = F \begin{pmatrix} s^{n+1,k} \\ c^{n+1,k} \end{pmatrix}, \tag{4b}$$

F being the nonlinear function defined by (3) and J its Jacobian, whose sparsity pattern is depicted in Fig. 1c.

We observe that second order accuracy can also be achieved by semi–implicit schemes (i.e. linearly implicit in the highest derivative terms) or performing only one iteration of Newton–Raphson at each time step. However, in the latter case, the numerical error would usually be higher than a fully implicit scheme, which in this case can be applied with very few Newton iterations (see e.g. Fig. 2).

Linear solver In practice, the linear system (4b) is not solved exactly, but its solution is approximated to sufficient precision with an iterative Krylov method. In particular here a preconditioned GMRES method is employed.

The preconditioner for the GMRES method is crucial in controlling the number of linear iterations and thus to keep low the computational cost of the method. The sparsity pattern of the Jacobian is illustrated in Fig. 1 for the 1D case; the 2D one can be obtained by tensor products. Moreover, [22] shows that the J_{cs} block is negligible and that an optimal preconditioner can be obtained by a block-upper-triangular first level preconditioner, followed by a multigrid preconditioner on J_{ss}. The efficiency

of the multigrid approach (see [3]) can be shown by using the notion of symbol and the related spectral results regarding Toeplitz and Generalized Locally Toeplitz sequences [15, 16]. In particular, with this approach, the number of GMRES iteration is constant when the grid size increases in both the uniform [22] and non-uniform [13] grid cases.

3.1 Accuracy and efficiency

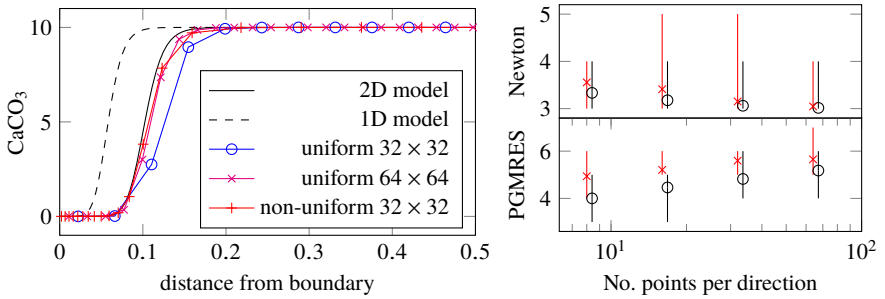

Fig. 2 (Left) $CaCO_3$ profiles with the 1D, the 2D model and the discretized 2D model. (Right) Nonlinear and linear iteration numbers versus grid size for uniform (black with circles) and non-uniform (red with crosses) Cartesian grids.

Second order accuracy for this method has been shown in [22, 13]. Moreover, in [13] a detailed study on the efficiency of the Newton and of the preconditioned GMRES (PGMRES) procedures was conducted, considering the cases of Cartesian domains discretized with uniform and non uniform grids. Fig. 2 reports the main results. In the left part we show the profiles of a converged numerical solution of (2) along the diagonal of the square (solid line) and the result predicted by the one-dimensional model applied along the same line, with the same physical parameters (dashed). The large gap between the two solutions indicated the importance of the two-dimensional effects in this situation. The numerical solutions computed with very coarse grids (lines with symbols) instead highlight the benefits of using non-uniform grids: the 32×32 non-uniform solution (red with plus sign) has almost the same accuracy of the much more costly 64×64 uniform solution (magenta with crosses). From the graph in the right part it can be appreciated that in all cases the number of nonlinear (Newton) and of linear (PGMRES) iterations do not vary significantly when the grid size is increased, both in their mean values (symbols) and in their ranges (whiskers).

4 Numerical approximation for arbitrary domains

In order to approximate numerically the solutions of (1) in more general domains, one could resort to finite element approximations, but the task of obtaining good quality meshes from scan data of real works of art seems formidable. We thus take another approach and we first lay a Cartesian grid with step h on the domain Ω, as shown in Fig. 3a. At each grid point P_{ij}, the values of the two unknown functions at time t^n are represented by the variables s_{ij}^n and c_{ij}^n.

Grid setup The task of the numerical method is to compute the values of the unknowns inside Ω, i.e. at the blue points in Fig. 3a. Their number is $O(1/h^d)$ in d spatial dimensions. Spatial discretization can be obtained as in (2), with the obvious simplifications since the s and c variables are now co-located at each grid node (see [10] for details), and they involve also the unknowns for another layer of points (red ones in Fig. 3a). These latter are $O(1/h^{d-1})$ and thus adding them to the system does not significantly affect its size.

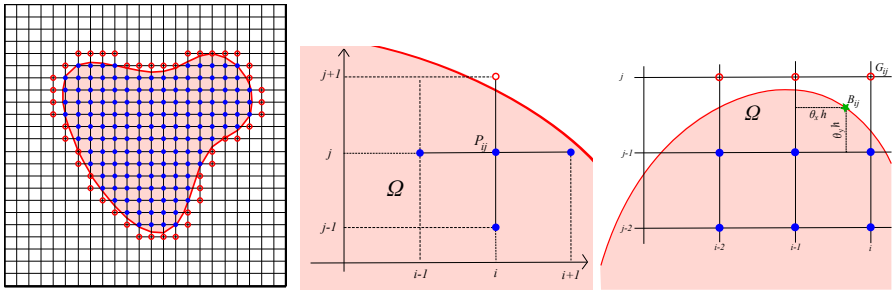

(a) (b) (c)

Fig. 3 (a) Co-located level-set approach of [10]. Internal grid points Ω_h (blue filled circles) and ghost points Γ_h (red empty circles). (b) Five-point stencil for L_h^s. (c) Nine-point stencil (red filled circles) associated with the ghost point G_{ij} to discretize the boundary conditions at B_{ij}.

Boundary conditions In [10] we considered a level-set technique to represent the computational domain. In this approach Ω is defined as the set of points in $\mathbb{R}^d$ such that $\varphi(\mathbf{x}) < 0$ for some real-valued function $\varphi : \mathbb{R}^d \to \mathbb{R}$ and its boundary $\partial\Omega$ is of course the set of points such that $\varphi(\mathbf{x}) = 0$. In particular, $\varphi(\mathbf{x})$ could have the absolute value equal to the distance of the point $\mathbf{x}$ from the closest point on $\partial\Omega$ and its sign could be set negative if $\mathbf{x}$ is inside the domain and positive otherwise. In this case, φ is called a *signed distance function* and since it is always possible to reduce to this situation, at least in a neighbourhood of the boundary, we will describe the method assuming that φ is a signed distance.

Let φ_{ij} be the value of φ at a grid point. All grid points such that $\varphi_{ij} < 0$ are inside the physical domain (blue points in Fig. 3a); the operators L_h^s and L_h^c are defined as in (2) for them. The computation of L_h^s and L_h^c for internal points involves

also their first neighbours, but these latter may be located outside of Ω (see Fig. 3b). The extra points involved in the discretization are called *ghost points* (red ones in Fig. 3a). For each ghost point, the definition of L_h^s and L_h^c is thus augmented with an equation that links the s and c values at ghost point with those in the interior domain, as follows. For a ghost point G_{ij}, first a 3×3 stencil involving only ghost and interior points is sought and the projection B_{ij} of G_{ij} on the boundary $\partial\Omega$ is approximated by using the values φ_{ij} and finite difference approximations of the gradient of φ (see Fig. 3c). Next, a biquadratic polynomial interpolating the values of the 9 points is formally computed. Finally, imposing the boundary conditions (e.g. point values, normal derivative, etc) at B_{ij} yields the relation that is added to the definition of the spatial operators. We point out that the 3×3 stencil of a ghost point may contain also other ghost points and thus that in this approach it is not possible to eliminate the boundary conditions from the system, whose final size will be $N_I + N_G$ where N_I and N_G are the numbers of inner and ghost points, respectively.

Nonlinear and linear solvers We apply the Newton-Raphson method to the non-linear system as in §3 and a tailored geometric multi-grid approach to solve the linear system of each Newton–Raphson iteration. An alternative approach (under investigation by the authors) is the application of a multigrid method to the entire non-linear system to possibly improve efficiency, such as FAS methods [24]. Finally, we point out that the prolongation, restriction and smoother must take into account the levelset in nodes close to the boundary, as explained in [10, 9, 7, 8].

4.1 Accuracy test

In order to test the accuracy, we modify the numerical method to solve a more general problem by adding source terms $f_s, f_c : \Omega\times[0,T] \to \mathbb{R}$ to the equations (1) for s and c respectively and a non-trivial boundary condition for $\frac{\partial c}{\partial n} = g_c(\mathbf{x},t)$. We choose f_s, f_c and the boundary conditions in such a way that the exact solutions are $s^{\mathrm{exa}}(\mathbf{x},t) = 2 + \sin(x)\cos(y)\sin\left(t+\sqrt{2}\right)$ and $c^{\mathrm{exa}}(\mathbf{x},t) = 3 + \sin(x/2)\cos(3y)\sin\left(2t+\sqrt{3}\right)$, so that we can easily compute the errors at time $t = 1$ on the solutions and on their gradients.

In Table 1 we show the result for a case when the domain is represented by the union of a square and four circles centred on the vertices. In particular we use the levelset function

$$\begin{aligned} \varphi(x,y) &= \min\{\varphi_1(x,y), \varphi_2(x,y),\} \\ \varphi_1(x,y) &= \max\{|x|,|y|\} - L, \\ \varphi_2(x,y) &= \sqrt{(|x|-L)^2 + (|y|-L)^2} - D, \end{aligned} \tag{5}$$

where $L = 0.9567$ and $D = 0.3$. Second order convergence is achieved for both variables. We refer to [10] for more complete data, showing that second order is achieved also in the gradients of both variables, and then that the accuracy of the method of [22, 13] is not degraded by the level-set approach. However, it is worth

Table 1 Accuracy test for the solution for s (SO_2) and c ($CaCO_3$) variables in the geometry shown at the left.

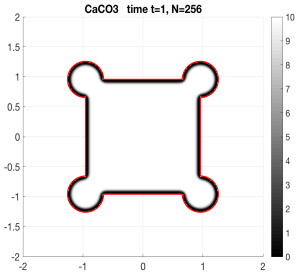

No. of points	$\|\mathbf{s}-\mathbf{s}^{\text{exa}}\|_1$ error	rate	$\|\mathbf{c}-\mathbf{c}^{\text{exa}}\|_1$ error	rate
16×16	$1.54\cdot10^{-2}$	–	$5.88\cdot10^{-3}$	–
32×32	$1.40\cdot10^{-3}$	3.46	$1.06\cdot10^{-3}$	2.47
64×64	$1.27\cdot10^{-4}$	3.46	$2.30\cdot10^{-4}$	2.20
128×128	$3.61\cdot10^{-5}$	1.81	$5.52\cdot10^{-5}$	2.06
256×256	$7.39\cdot10^{-6}$	2.29	$1.35\cdot10^{-5}$	2.03

to point out that the second order accuracy might be degraded for real problems close to boundary singularities. This degradation is not observed here since an artificial solution is adopted. To resume second order accuracy overall, the authors are investigating the implementation of adaptive grids that are properly refined in the vicinity of singular boundaries.

4.2 Efficiency of solvers

In order to study the multigrid performance, we solved Eq. (1) with the following initial and boundary conditions: $s_0(\mathbf{x}) = 0$, $c_0(\mathbf{x}) = 10$ and $g_s = 1$. The domain is defined by Eq. (5) and is shown at the left of Table 1(see also [10]). Solutions are computed up to time $t = 1$ and for each W-cycle of the multigrid method, we compute the convergence factor as:

$$\rho_{\text{MG}}^{(q)} = \left\|\mathbf{r}_h^{(q)}\right\|_\infty \Big/ \left\|\mathbf{r}_h^{(q-1)}\right\|_\infty,$$

where

$$\mathbf{r}_h^{(q)} = \begin{bmatrix}\mathbf{r}_h^s\\ \mathbf{r}_h^c\end{bmatrix} = \begin{bmatrix}F^s(W^{(n+1,k)}) - \left(J^{ss}(W^{(n+1,k)})\cdot\Delta\mathbf{s} + J^{sc}(W^{(n+1,k)})\cdot\Delta\mathbf{c}\right)\\ F^c(W^{(n+1,k)}) - \left(J^{cs}(W^{(n+1,k)})\cdot\Delta\mathbf{s} + J^{cc}(W^{(n+1,k)})\cdot\Delta\mathbf{c}\right)\end{bmatrix}$$

is the defect after q W-cycles. Convergence factors for each multigrid iteration, plotted in Fig. 4, are lower than or close to $\rho = 0.119$, which is the predicted value by the Local Fourier Analysis for scalar multigrid in rectangular domains [24, Table 4.1, page 117], showing that the multigrid efficiency has not been degraded by the non-rectangular domain and the level-set ghost-point approach.

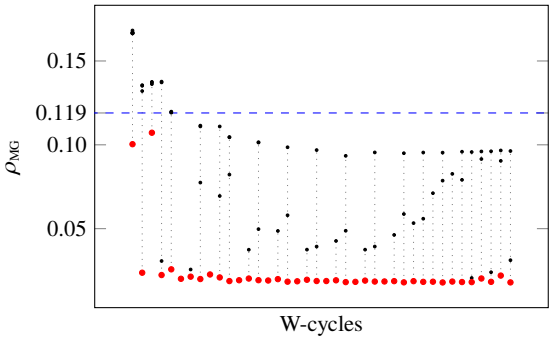

Fig. 4 Convergence factors of the first 40 W-cycle iterations on the problem of Table 1. Larger red markers highlight the convergence factor of the first W-cycle for each linear system. The dotted vertical lines connect all convergence factors observed for the same linear system.

4.3 Domains defined by images

In real-world cases one would need to define a level-set function from image data, for example from three-dimensional laser scans. Here, merely in order to show the possibilities of our numerical approximation technique, we apply it to the case of a level-set function defined from a two-dimensional pixelated image depicting the head of a raindeer.

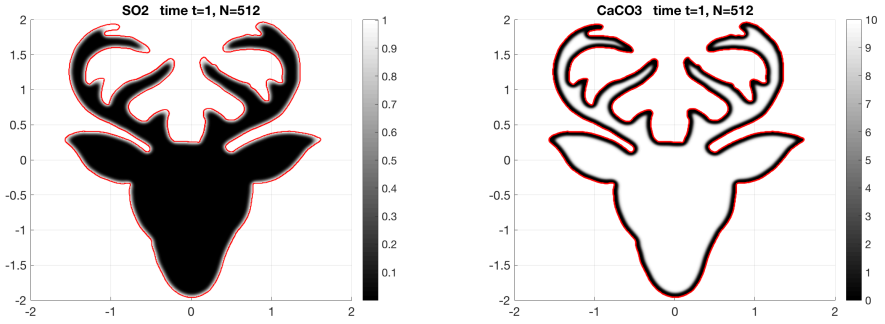

Fig. 5 Solutions for the raindeer test at time $t = 1$ with $N = 512$.

More precisely, we define a provisional level-set by setting $\phi = -1$ inside the domain and $\phi = 1$ outside the domain, making the boundary stepwise. To correct that, the level-set function is slightly diffused (two iteration steps of diffusion equation). After the diffusion, the steps disappear without affecting the important features of the domain. This procedure suffices to produce a smooth enough level-set function for this academic test case. In real applications, which are part of our ongoing effort, a more rigorous procedure can be used to obtain an accurate level-set representation of the monument.

The computational domain and the solution at final time are depicted in Fig. 5. It is evident that in regions with a high curvature of the boundary there is a faster

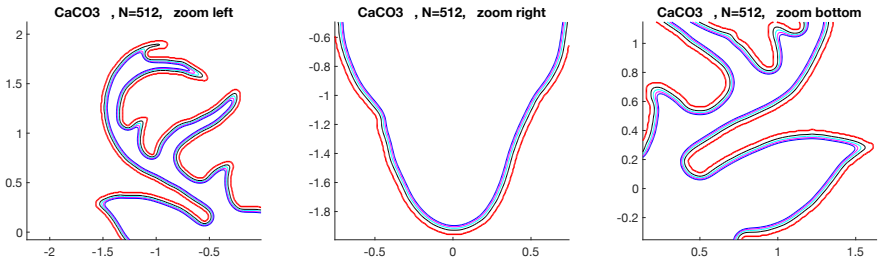

Fig. 6 Contour plot of $c = 5$ ($CaCO_3$) for the raindeer test at times $t = 0.25$, $t = 0.5$, $t = 0.75$ and $t = 1$. The boundary of the domain is the red most external line, while the four contour lines can be easily recognised as they move away from the boundary as t increases; they are colored in black ($t = 0.25$), cyan ($t = 0.5$), magenta ($t = 0.75$) and blue ($t = 1$).

growth of the gypsum crust (e.g. the horns, the ear tips), while the crust grows more slowly near more rounded features (e.g. the chin). Note also that the original image is slightly asymmetric, in particular at the highest tips of the horns, which results in a very different evolution of the tips of the left and right horns.

The time evolution is depicted in Fig. 6 for the left horn, the chin and the right ear. The different speed of propagation of the gypsum front is very evident here. Note for example that the uppermost tip of the horn has completely disappeared at a very early time, while for example the tip of the ear simply gets more rounded as time goes by, while at the chin the propagation front does not significantly change its shape while retracting.

5 The tickness of the gypsum crust as a function of the curvature

In view of the remarks about the propagation speed of the gypsum front in the previous test, we test numerically the asymptotic results on the thickness $\xi(t)$ of the gypsum crust that were proven in one space dimension by [2] and then confirmed by experimental data in [17, 23]:

$$\xi(t) \sim C\sqrt{t} \tag{6}$$

In this section we test numerically this law in two space dimensions, showing that the constant C in the scaling law is influenced by the curvature of the monument, in agreement with the well-known connection between diffusion equations and motion by mean curvature, studied by many authors [18, 19, 14].

Infinite slice In the first test, the monument is represented by an infinite slice $-R \le x \le R$, $-\infty < y, z < \infty$, reducing to the 1D problem where (1) is solved in the domain $\Omega = [-R, R]$.

At each time step t_n, we approximate the interface $\Gamma(t_n)$ separating the gypsum crust from the rest of the monument by solving the nonlinear equation

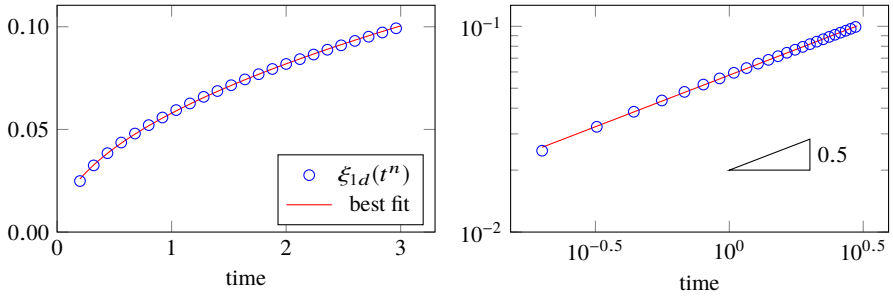

Fig. 7 Numerical tests on an infinite slab. Time evolution of the crust thickness $\xi(t)$ (blue circles) and best fit approximation $\xi(t) = C\sqrt{t}$ (red solid line) for $R = 0.2$. Left: linear axis scale. Right: bilogarithmic scale.

$$c(\Gamma(t_n), t_n) = c_0/2,$$

using the bisection method, where $c_0 \in \mathbb{R}$ is the initial value of calcium carbonate in the whole monument. The thickness of the gypsum crust at time t_n is then approximated by

$$\xi(t_n) = R - \Gamma(t_n).$$

In order to validate the scaling law (6), we assume that $\xi(t)$ can be expressed as $\xi(t) = C\,t^p$, which implies $\log \xi(t) = \log C + p \log t$. Then, we find the best fit line $Y = \alpha + \beta X$ that approximates in the least-squares sense the data $(X_n, Y_n) = (\log t_n, \log \xi(t_n))$ and then determine $C = 10^\alpha$ and $p = \beta$. The tests are performed with $N = 512$ grid points. In Fig. 7 we plot the best fit line and the data (X_n, Y_n). We have $p \approx 1/2$, as in the scaling law (6), and for the values of the model parameters listed in §1, the value of the constant is $C_{1D} = 0.0579$.

Infinite cylinder Next, in order to investigate on the two-dimensional effects on the scaling law (6), we consider a monument constituted by an infinite cylinder $x^2 + y^2 \le R^2$, $-\infty < z < \infty$, which can be represented by the two-dimensional problem (1) on the circle $\Omega = \{x^2 + y^2 \le R^2\}$.

For different values of R, the numerical solution is computed with 512×512 grid points. At each time step t_n, the interface $\Gamma(t_n)$ is approximated by a discrete set of points (x_k, y_k), $k = 1, \ldots, N_\Gamma$, that are found by solving, for each $k = 1, \ldots, N_\Gamma$, the nonlinear equation $g(r) := c(\mathbf{x}(r, \theta_k), t) - c_0/2 = 0$, where $\mathbf{x}(r, \theta_k) = (r\cos\theta_k, r\sin\theta_k)$ and $\theta_k = 2\pi k / N_\Gamma$. The numerical solution $\tilde{r}$ of the nonlinear equation is obtained by the bisection method with an accuracy of h^2. The function evaluations $g(r)$ are performed by biquadratic interpolation. Finally, we set $(x_k, y_k) := \mathbf{x}(\tilde{r}, \theta_k)$.

The interface $\Gamma(t)$ is expected to be a circle centred at the origin with a radius smaller than R. The average thickness of the gypsum crust at time t_n is then approximated by

$$\xi(t_n) = R - \frac{1}{N_\Gamma} \sum_{k=1}^{N_\Gamma} \sqrt{x_k^2 + y_k^2}.$$

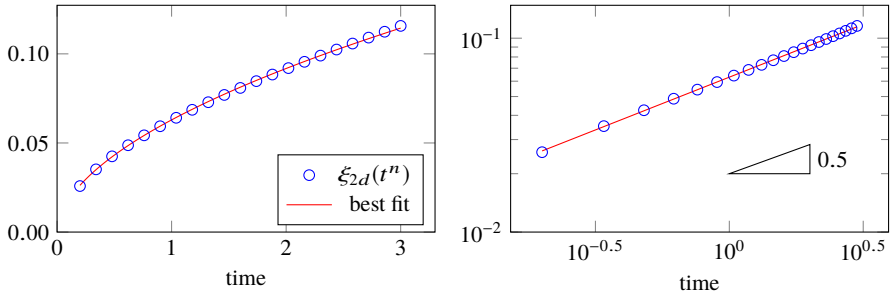

Fig. 8 Numerical tests on an infinite cylinder. Time evolution of the crust thickness $\xi(t)$ (blue circles) and best fit approximation $\xi(t) = C(R)\sqrt{t}$ (red solid line) for $R = 0.2$. Left: linear axis scale. Right: bilogarithmic scale.

In Fig. 8 we plot the time evolutions of the thickness for $R = 0.2$.

Table 2 Best fit values of the scaling law $\xi(t) = C\,t^p$ for various values of the radius R.

R	0.0910	0.1183	0.1538	0.2000	0.2600	0.3380	0.4394	0.8000	2.0000
p	0.4917	0.489	0.4882	0.4856	0.4879	0.4852	0.4821	0.4838	0.4838
C	0.0829	0.0698	0.0652	0.0629	0.0614	0.06	0.0587	0.0587	0.0581

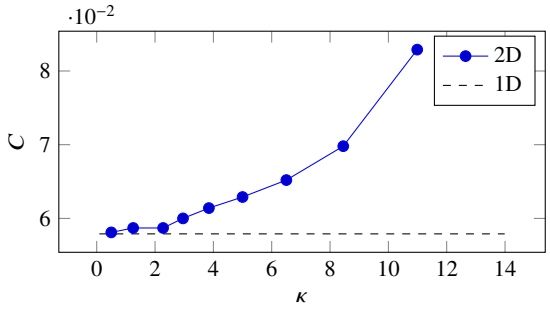

Fig. 9 C against curvature $\kappa = 1/R$ for the infinite cylinder. The horizontal solid line represents the value of $C_{1D} = 0.0579$.

A similar situation is observed for other values of the radius. The values p and C found for all tested values of R are reported in Table 2. We observe that $p \approx 1/2$ independently on R, showing that the scaling law (6) is correct also in higher dimensions, but that the constant C depends on the radius. From Fig. 9 it can be appreciated that C is an increasing function of the mean curvature $\kappa = 1/R$ (i.e. a decreasing function of the radius), converging to C_{1D} when $\kappa \to 0$ (i.e. $R \to \infty$). Fig. 9 suggests also that the relation between C and κ is more than linear, although further investigation of the connection between the diffusion processes of the current

problem and motions by mean curvature, from both the analytical and numerical point of views, would be needed in order to identify a more accurate expression.

6 Conclusions

In this chapter we have presented our work on computing numerical solutions for a model of gypsum crust formation on marble monuments. For globally Cartesian domains we have shown the optimal efficiency of a finite difference method, joined with Newton-Raphson nonlinear solves and GMRES linear solvers preconditioned with multigrid techniques, both for uniform and non-uniform meshes. For general domains we have successfully applied an approach that describes the computational domain on a uniform Cartesian grid with the help of a level-set function and modifies accordingly the spatial discretization and the multigrid techniques.

It is important to note that, although surface meshes of works of art can be obtained from laser scan data, these often turn out to be of bad quality for finite element computations and automating their extrusion to a good quality simplicial volume mesh does not appear feasible. On the other hand it seems much easier to compute a good quality levelset function from the laser scan data, keeping in mind that ϕ ought to be a signed distance only in the immediate neighbourhood of the surface. We are conducting further research in this direction.

The method presented in this chapter is thus promising for real-world computations with differential models on works of art. In order to deal with a real-world three-dimensional case, however, it will be almost mandatory to supplement the levelset method with local grid refinement capabilities, as crust formation models clearly have solutions that significantly vary only in the neighbourhood of the monument surface.

It is also expected that these numerical techniques will prove useful in computing the solution of more complex PDE models, like the gypsum model with swelling of [6] and the copper corrosion model of [5].

References

1. Alì, G., Furuholt, V., Natalini, R., Torcicollo, I.: A mathematical model of sulphite chemical aggression of limestones with high permeability. part i. modeling and qualitative analysis. Transp. Porous Media **69**(1), 109–122 (2007). DOI 10.1007/s11242-006-9067-2
2. Aregba Driollet, D., Diele, F., Natalini, R.: A mathematical model for the SO_2 aggression to calcium carbonate stones: numerical approximation and asymptotic analysis. SIAM J. Appl. Math. **64**(5), 1636–1667 (2004)
3. Aricò, A., Donatelli, M., Serra-Capizzano, S.: V-cycle optimal convergence for certain (multilevel) structured linear systems. SIAM J. Matrix Anal. Appl. **26**(1), 186–214 (2004). DOI 10.1137/S0895479803421987. URL https://doi.org/10.1137/S0895479803421987

4. Bonetti, E., Cavaterra, C., Freddi, F., Grasselli, M., Natalini, R.: A nonlinear model for marble sulphation including surface rugosity: theoretical and numerical results. Comm. Pure Appl. Anal. **18**(2), 977–998 (2019). DOI 10.3934/cpaa.2019048
5. Clarelli, F., De Filippo, B., Natalini, R.: Mathematical model of copper corrosion. Appl. Math. Model. **38**(19-20), 4804–4816 (2014). DOI 10.1016/j.apm.2014.03.040
6. Clarelli, F., Fasano, A., Natalini, R.: Mathematics and monument conservation: Free boundary models of marble sulfation. SIAM J. Appl. Math. **69**(1), 149–168 (2008). DOI 10.1137/070695125
7. Coco, A., Currenti, G., Del Negro, C., Russo, G.: A second order finite-difference ghost-point method for elasticity problems on unbounded domains with applications to volcanology. Communications in Computational Physics **16**(4), 983–1009 (2014)
8. Coco, A., Russo, G.: Finite-difference ghost-point multigrid methods on cartesian grids for elliptic problems in arbitrary domains. Journal of Computational Physics **241**, 464–501 (2013)
9. Coco, A., Russo, G.: Second order finite-difference ghost-point multigrid methods for elliptic problems with discontinuous coefficients on an arbitrary interface. Journal of Computational Physics **361**, 299–330 (2018)
10. Coco, A., Semplice, M., Serra Capizzano, S.: A level-set multigrid technique for nonlinear diffusion in the numerical simulation of marble degradation under chemical pollutants. Appl. Math. Comput. (in press). Preprint https://arxiv.org/abs/1902.07029
11. Di Turo, F., Proietti, C., Screpanti, A., Fornasier, M., Cionni, I., Favero, G., De Marco, A.: Impacts of air pollution on cultural heritage corrosion at european level: What has been achieved and what are the future scenarios. Environmental Pollution **218**, 586–594 (2016). DOI 10.1016/j.envpol.2016.07.042
12. Donatelli, M., Semplice, M., Serra-Capizzano, S.: Analysis of multigrid preconditioning for implicit PDE solvers for degenerate parabolic equations. SIAM J. Matrix Anal. **32**(4), 1125–1148 (2011)
13. Donatelli, M., Semplice, M., Serra-Capizzano, S.: AMG preconditioning for nonlinear degenerate parabolic equations on nonuniform grids with application to monument degradation. Appl. Numer. Math. **68**, 1–18 (2013)
14. Esedog, S., Tsai, Y.H.R., et al.: Threshold dynamics for the piecewise constant mumford–shah functional. Journal of Computational Physics **211**(1), 367–384 (2006)
15. Garoni, C., Serra-Capizzano, S.: Generalized locally Toeplitz sequences: theory and applications. Vol. I. Springer, Cham (2017). DOI 10.1007/978-3-319-53679-8. URL https://doi.org/10.1007/978-3-319-53679-8
16. Garoni, C., Serra-Capizzano, S.: Generalized locally Toeplitz sequences: theory and applications. Vol. II. Springer, Cham (2018). DOI 10.1007/978-3-030-02233-4. URL https://doi.org/10.1007/978-3-030-02233-4
17. Giavarini, C., Santarelli, M., Natalini, R., Freddi, F.: A non-linear model of sulphation of porous stones: Numerical simulations and preliminary laboratory assessments. J. Cultural Heritage **9**(1), 14–22 (2008). DOI 10.1016/j.culher.2007.12.001
18. Merriman, B., Bence, J.K., Osher, S.: Diffusion generated motion by mean curvature. Department of Mathematics, University of California, Los Angeles (1992)
19. Merriman, B., Ruuth, S.J.: Diffusion generated motion of curves on surfaces. Journal of Computational Physics **225**(2), 2267–2282 (2007)
20. Nikolopoulos, C.: Mathematical modelling of a mushy region formation during sulphation of calcium carbonate. Netw. Heterog. Media **9**(4), 635–654 (2014). DOI 10.3934/nhm.2014.9.635
21. Saba, M., Quiñones-Bolaños, E., Barbosa López, A.: A review of the mathematical models used for simulation of calcareous stone deterioration in historical buildings. Atmospheric Environment **180**, 156–166 (2018). DOI 10.1016/j.atmosenv.2018.02.043
22. Semplice, M.: Preconditioned implicit solvers for nonlinear PDEs in monument conservation. SIAM J. Sci. Comput. **32**(5), 3071–3091 (2010)
23. Skoulikidis, T., Papakonstantinou-Ziotis, P.: Mechanism of sulphation by atmospheric SO_2 of the limestones and marbles of the ancient monuments and statues: I. observations in situ (Acropolis) and laboratory measurements. British Corrosion Journal **16**(2), 63–69 (1981)
24. U.Trottemberg, Oosterlee, C., Schuller, A.: Multigrid. Academic Press (2000)